

# Mechanical Properties of Phosphorene Nanotubes: A Density Functional Tight-Binding Study

---

V. Sorkin\* and Y.W. Zhang†

Institute of High Performance Computing, A\*STAR, Singapore 138632

## Abstract

Using density functional tight-binding method, we studied the elastic properties, deformation and failure of armchair (AC) and zigzag (ZZ) phosphorene nanotubes (PNTs) under uniaxial tensile strain. We found that the deformation and failure of PNTs are very anisotropic. For ZZ PNTs, three deformation phases are recognized: The primary linear elastic phase, which is associated with the interactions between the neighboring puckers, succeeded by the bond rotation phase, where the puckered configuration of phosphorene is smoothed via bond rotation, and lastly the bond elongation phase, where the P-P bonds are directly stretched up to the maximally allowed limit and the failure is initiated by the rupture of the most stretched bonds. For AC PNTs, the applied strain stretches the bonds up to the maximally allowed limit, causing their ultimate failure. For both AC and ZZ PNTs, their failure strain and failure stress are sensitive while the Young's modulus, flexural rigidity, radial Poisson's ratio and thickness Poisson's ratio are relatively insensitive to the tube diameter. More specifically, for AC PNTs, the failure strain decreases from 0.40 to 0.25 and the failure stress increases from 13 GPa to 21 GPa when the tube diameter increases from 13.3 Å to 32.8 Å; while for ZZ PNTs, the failure strain decreases from 0.66 to 0.55 and the failure stress increases from 4 GPa to 9 GPa when the tube diameter increases from 13.2 Å to 31.1 Å. The Young's modulus, flexural rigidity, radial and thickness Poisson ratios are 114.2 GPa, 0.019 eV·nm<sup>2</sup>, 0.47 and 0.11 for AC PNTs, and 49.2 GPa, 0.071 eV·nm<sup>2</sup>, 0.07 and 0.21 for ZZ PNTs, respectively. The present findings provide valuable references for the designs and applications of PNTs as device elements.

*Keywords: phosphorene nanotubes, uniaxial tensile strain, failure mechanism, DFTB*

## 1. Introduction

---

\* Email address: sorkinv@ihpc.a-star.edu.sg

† Email address: zhangyw@ihpc.a-star.edu.sg

Phosphorene, a two-dimensional (2D) form of black phosphorus, has provoked significant interest lately due to its direct band-gap semiconducting features [1],[2],[3]. At first, multi-layer phosphorene was attained through mechanical exfoliation [4],[5],[6], and then monolayer phosphorene was obtained by plasma thinning process [7]. Phosphorene is a very appealing material in addition to graphene [8],[9], boron nitride [10],[11],[12], and transition metal dichalcogenides (TMDs) [13],[14],[15],[16]. Phosphorene is ideally suitable for field-effect transistors [17],[18],[19],[20],[21],[22], since it a direct band-gap semiconductor with a considerable fundamental band gap. Besides its direct band gap, phosphorene has a comparatively high direction-dependent carrier mobility, which can be considerably altered by applied straining [20],[23],[24],[25],[26],[27],[28],[29],[30],[31],[32]. Its thermal transport [33],[42], and mechanical properties are also highly anisotropic because of its puckered structure [34],[35], [36]. The wide diversity of electronic, mechanical and thermal properties under strain [19],[34],[31],[37],[38] make phosphorene a particularly appealing 2D material for strain engineering and flexible electronics [39],[40], [34],[23]. In addition, other fascinating applications of phosphorene have been demonstrated, such as gas sensors [41],[42],[43],[44], thermo-electrics [45],[46],[47],[48], anodes in Li-ion batteries [46],[49],[50], p-n junctions [51],[52],[53], photo-catalysts [25] and components of solar-cell devices [21],[24],[54].

Along with phosphorene, of prime importance are phosphorene-based nanostructures, which are potential building blocks for a large variety of technological applications from sensing devices to active optoelectronic elements [1]. Phosphorene nanoribbons, nanotubes and fullerene-like structures, just as graphene nanoribbons, carbon nanotubes and fullerenes are currently the subject of intensive research [1],[2]. For example, comprehensive theoretical studies have been carried out to explore the electronic and mechanical properties of phosphorene nanoribbons. It was found that phosphorene nanoribbons can be either metals (with zig-zag edges) or semiconductors (with arm-chair edges). The band gap of arm-chair nanoribbons can be tuned by strain [24], electric field [55],[56],[57], chemical functionalization [50],[58],[59] and edge passivation [55],[60]. Though not as mechanically tough as graphene, boron-nitride or TMD-based nanoribbons as might be hoped, the in-plane stiffness of phosphorene nanoribbons is still much larger than that of many commonly used materials [34], [35], [36].

Phosphorene nanotubes (PNTs) and fullerene-like nanoparticles are less explored. For example, research has been conducted to study the electronic properties of PNTs [55],[61]. It was found that PNTs are direct band gap semiconductors. The electronic properties of PNTs can be tuned from semiconducting to metallic by applying strain or electric field [55]. PNTs can be formed by deforming monolayer phosphorene at substantial strain energy cost. Guan et al. [62] suggested that this energy cost can be avoided by forming faceted nanotubes using a variety of stable planar phases of phosphorene, which can be connected at essentially zero energy cost. This option to mix different phases offers exceptional richness in PNT forms and their associated properties [62].

While some of the elastic properties of phosphorene nanotubes have been studied [61], their deformation and failure mechanisms at large strain, however, are mostly unexplored. This is in strong contrast with the significant amount of works performed on other 2D materials, such as graphene [63],[64],[65],[66],[67], boron-nitride [68],[69],[70],[71] and dichalcogenides nanotubes

[14],[72],[73],[74]. The behavior of PNTs under straining, in particular, their deformation and failure mechanisms and their critical strain and stress, must have been studied comprehensively in order to use PNTs in upcoming nano-mechanical devices.

Our goal is to investigate the structural properties, deformation and failure of armchair and zigzag PNTs under large uniaxial tensile straining. Our objective is to find the answers for the following questions: What are the fracture mechanisms of PNTs? Does their puckered structure profoundly affect the deformation and failure? Is there an evident mechanical anisotropy in PNTs? Are the failure strain and strength dependent on the geometry and the diameter of PNTs? To answer these questions, we carry out density functional tight binding calculations, concentrating on the two primary geometries of nanotubes: armchair (AC) and zigzag (ZZ) phosphorene nanotubes.

## 2. Computational Model

Single-wall AC and ZZ PNTs can be constructed by rolling up phosphorene monolayer along the AC and ZZ directions (see Figure 1). The constructed geometries can be described by the number of phosphorene unit cell aligned along the nanotube circumference.

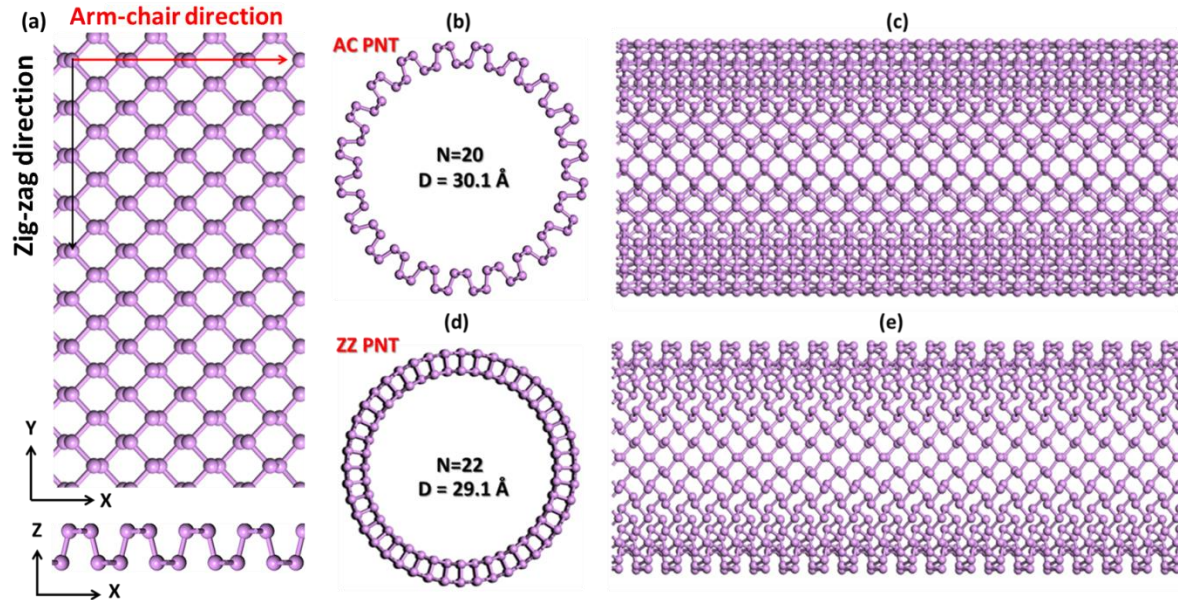


Figure 1: (a) Upper panel (top view): phosphorene monolayer with the AC (along the X-axis) and ZZ (along the Y-axis) directions indicated. Lower panel (side view): puckered structure of phosphorene. (b, c) AC phosphorene nanotube with diameter  $D = 30.1 \text{ \AA}$  ( $N=20$ , where  $N$  is the number of unit cell aligned along the nanotube circumference): top (b) and side (c) views; (d, e) ZZ phosphorene nanotube with diameter  $D = 29.1 \text{ \AA}$  ( $N=22$ ): top view (d) and side view (e).

We apply tight-binding (TB) technique [75],[76],[77],[78] to examine the deformation and failure of PNTs under uniaxial tensile strain. The TB technique has a special place among the computational

techniques accessible for nanoscale modelling of materials. On one hand, the density function theory (DFT) method, which has been extensively used to explore nanoscale phosphorene-based systems, is very precise, but computationally demanding. As a result, the DFT calculations are not feasible for large or even intermediate scale systems. On the other hand, molecular dynamics (MD) simulations cannot be used either since trustworthy, highly-reliable and widely accepted interatomic potential for phosphorene is yet not available. In this situation, empirical tight-binding technique, situated in between DFT and MD in terms of computational cost and accuracy, is an ideal approach to deal with the size problem.

In our simulations of PNTs, we apply density functional tight-binding (DFTB) method [79], which appropriately combines the accuracy of DFT with the computational effectiveness of TB. The DFTB is derived from DFT but uses empirical approximations to increase the computational efficiency, while preserving accuracy [80], [81], [82]. The substitution of the many-body Hamiltonian of DFT with a parameterized Hamiltonian matrix is the key approximation in the TB method [83]. In the DFTB approach, quasi-atomic wave functions, represented in terms of Slater-Koster type orbitals [75] and spherical harmonics [84], are applied to model the electron density. The orbital basis is created and fitted using DFT calculations, and then applied to calculate the Hamiltonian and overlap matrix elements [79]. These matrix elements do not completely define the total energy of the system. The residual part of the total energy is added as a short-range repulsive term, which can be represented in terms of pair wise potentials between atoms. The pair wise potentials are obtained via a fitting routine. Besides the short-range and electronic repulsive terms, the Kohn-Sham energy contains the dispersion interactions (van der Waals forces) and Coulomb interactions [79]. At a long distance, the second term describes long-range electrostatic interactions between two point charges and also includes self-interaction contributions of a given atom (if the charges are positioned at the same atom) [85].

Furthermore, one uses self-consistent charge (SCC) technique in DFTB to improve the description of atom bonding [85]. Due to the SCC extension, the DFTB can be effectively applied to problems where shortages in the non-SCC standard TB method come to be evident [79]. Combining almost quantum mechanical precision and computational efficiency similar to molecular dynamics methods, the DFTB comes up with exceptional opportunities to explore nano-systems inclosing a few hundreds of atoms. For instance, structural, mechanical and electronic properties of phosphorene monolayer, nanoribbons, and nanotubes were investigated earlier by using DFTB [61],[27],[56],[86],[87],[88],[89].

Following our previous approach in DFTB simulations [89],[90] optimized the unit cell of phosphorene found by DFT method [21]. Using the DFTB optimized unit cell, we constructed a phosphorene monolayer and rolled it up into the AC (see Figure 1(a)) and ZZ (see Figure 1(b)) PNTs. In what follows, we investigate the mechanical response of PNTs with different diameters (see Figure 2) exposed to uniaxial tensile strain. By varying the number of unit cells along the nanotube circumference from  $N=8$  to  $N=22$ , we constructed AC PNTs with the diameter in the range from  $D=13.3 \text{ \AA}$  to  $D=32.8 \text{ \AA}$ , and ZZ PNTs from  $D=13.2 \text{ \AA}$  to  $D=31.1 \text{ \AA}$ . The length of the AC and ZZ PNTs was chosen to be  $L=14.8 \text{ \AA}$  and  $L=16.4 \text{ \AA}$ , respectively. In order to check the effect of nanotube length, we doubled the length and found that the obtained results for the shorter nanotubes did not deviate significantly from the longer ones. The total number of atoms used in our DFTB simulations varied in the range between  $\sim 100$  to  $\sim 350$ .

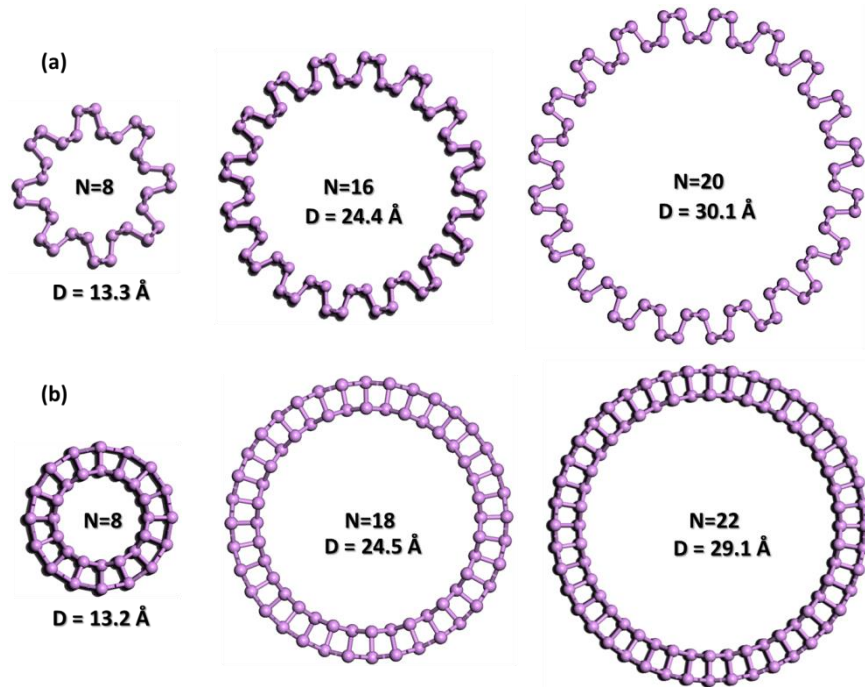


Figure 2: (a) DFTB optimized AC PNTs with different diameters:  $D = 13.25 \text{ \AA}$  ( $N=8$ ),  $D = 24.44 \text{ \AA}$  ( $N=16$ ) and  $D = 30.05 \text{ \AA}$  ( $N=20$ ). (b) DFTB optimized ZZ PNTs with different diameters:  $D = 13.22 \text{ \AA}$  ( $N=8$ ),  $D = 22.26 \text{ \AA}$  ( $N=18$ ) and  $D = 29.06 \text{ \AA}$  ( $N=22$ ). Here,  $N$  is the number of unit cell along the tube circumference.

In our DFTB simulations, we enforced periodic boundary conditions in all directions. The uniaxial strain was applied along the nanotube axis (X-axis). To avoid the self-interaction of PNTs due to periodic boundary conditions along the Y and Z axes, a vacuum slab was added in the radial directions perpendicular to the tube axis. The width of the vacuum slab was chosen to be  $20 \text{ \AA}$ . The k-point set for the Brillouin-zone integration was chosen by using the Monkhorst-Pack method [91],[92],[95]. The Monkhorst-Pack grid [91],[92] with an  $8 \times 2 \times 2$  sampling set was adapted for Brillouin-zone integration. Following the DFTB studies for PNTs [61], the s- and p-orbitals were specified for every P-atom. The Slater-Koster files [75] for phosphorus atoms were taken from ‘MATSCI’ set [93],[94].

We applied a uniform uniaxial tensile strain to the PNTs quasi-statically along the tube axis (X-axis) at zero temperature. The tensile strain was increased gradually by a small step of  $\delta\epsilon=0.01$ . Consequently, the initial configuration of the PNTs was relaxed by minimizing the total energy of the system using conjugate gradient method. The self-consistent charge calculations were carried out at each step of the energy minimization. We estimated a nominal stress, as explained in [21], calculating the force per unit cross-sectional of effective area of the PNT, which is obtained as the difference between the areas of the outer and inner circles, outlined by the outer and inner radii of the PNT (see Figure 2).

## 3. Results and Discussion

### 3.1 Geometry optimization

As the first step, we optimized the geometry of the constructed PNTs by minimizing their total potential energy. After the relaxation of the PNT structures, we obtained the tube diameters and lengths at zero strain. Both the bond lengths and bond angles in the phosphorene sheet have to be changed to accommodate for the tube curvature. In monolayer phosphorene, P-atoms are linked in a ring-like structure (see Figure 1). Each ring consists of six P-atoms, similar to the hexagonal ring in graphene. Yet, unlike graphene, phosphorene is not perfectly flat; instead, due to the  $sp^3$  hybridization, the P-atoms form a nonplanar puckered (folded) accordion-like structure, resembling a hexagonal atomic plane under compression. This puckered structure maximizes the distance between the lone electron pairs located at each P-atom [61][61][61],[57],[58]. Each phosphorene atom is connected to the three nearest neighbors by covalent bonds as shown in Figure 3(a). The two of its neighbors are in the same [XY] plane, and together they form an angle of  $\theta=96.16^\circ$ . The third neighbor is located in the adjacent plane at the angle  $\gamma=102.42^\circ$  (see Figure 3(a)). The bond length between the adjacent in-plane atoms (denoted as the **A**-bond in Figure 3(a)) is somewhat shorter than the bond length between the nearest atoms located in different planes (denoted as the **B**-bond in Figure 3(a)). The lengths of the A-bonds located in the lower or upper plane are the same.

When a phosphorene sheet is rolled into a tube, the symmetry between the lower and upper planes and the corresponding equivalence of the bond length, are broken. The bond length of the A-bonds in the inner shell (denoted as  $A_I$  bonds in Figure 3, where the subscript *I* denotes the inner tube shell) shortens; while the bond length of the A-bonds in the outer shell (denoted as  $A_O$  bonds in Figure 3, where the subscript *O* denotes the outer tube shell) lengthens. Apparently, the degree of the bond length contraction or elongation depends on the tube diameter, similar to carbon nanotubes [96],[97],[98],[99],[100]. The differences between the inequivalent bonds increase with the decrease in the tube diameter. The bond lengths of the  $A_I$ ,  $A_O$  and B-bonds as a function of tube diameter at zero strain are shown in Figure 4(a) for AC and Figure 4(b) for ZZ PNTs. The differences in the bond length between the PNT and phosphorene monolayer are clearly visible. As expected, the bond length of the inner  $A_I$  bonds decreases significantly, while the bond length of the outer  $A_O$  bonds increases evidently with the tube diameter. The bond length contraction for the inner  $A_I$  bonds is more evident for AC PNTs than for ZZ PNTs. The difference between the  $A_I$  and  $A_O$  bonds also increases with the decrease in the tube diameter. Both the effects of bond length contraction and elongation can be understood in terms of the curvature-induced re-hybridization of P-P orbitals [61].

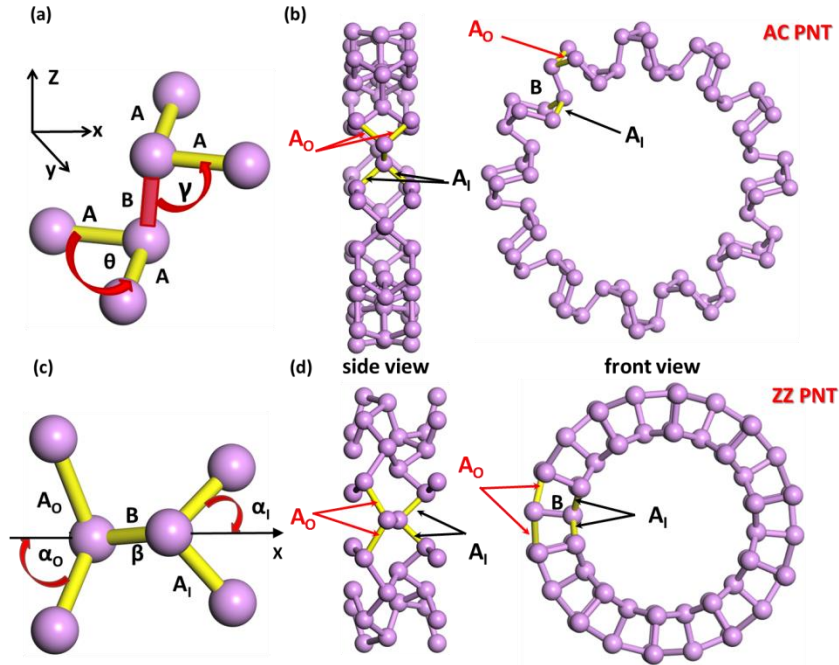


Figure 3: (a) Two types of P-P bonds in puckered monolayer phosphorene: the B-bond marked by red and A-bonds marked by yellow. (b), (d) A-bonds situated in the outer ( $A_0$ -bonds, red arrows) and inner shell ( $A_1$ -bonds, black arrows) of AC (b) and ZZ (d) PNTs. Side and front views are used to illustrate the positions of the bonds. (c) Angles  $\alpha_i$ ,  $\alpha_o$ ,  $\beta$  between  $A_1$ -bond,  $A_0$ -bond, B-bond and the stretching direction (X-axis), respectively.

The length of the B-bonds, which connect to the  $A_1$  and  $A_0$  bonds, similarly depends on the tube diameter. In the case of AC PNTs, the length of B-bonds, which are oriented at a right angle to the direction of the applied strain, is noticeably larger than that of phosphorene monolayer. It decreases monotonously with the tube diameter, and finally converges to that of phosphorene monolayer. In contrast, for ZZ PNTs, the length of the B-bonds at smaller tube diameters is shorter than in phosphorene monolayer. It increases evenly with the tube diameter, and finally converges to bond length of phosphorene monolayer (see Figure 4).

Besides the change in the bond length, there is a slight bond reorientation. In what follows, we examined the angles between the stretching direction and nanotube bonds. Three angles,  $\alpha_i$ ,  $\alpha_o$ , and  $\beta$ , which are the angles between the  $A_1$ -,  $A_0$ - and B-bonds and stretching direction (X-axis), are exemplified in 3(c). As shown in Figure 4(c), the  $A_1$  and  $A_0$  bonds in AC PNTs are arranged at an acute angle ( $\alpha_i, \alpha_o \approx 45^\circ$ ), while the B-bonds are approximately normal to the stretching direction ( $\beta \approx 90^\circ$ ). The values of these angles are unaffected by the AC tube diameter. On the contrary, the  $A_1$  and  $A_0$  bonds of ZZ PNTs are arranged at two different angles ( $\alpha_i \approx 45^\circ$  and  $\alpha_o \approx 55^\circ$ ), while the B-bonds are aligned at an acute angle ( $\beta \approx 75^\circ$ ) to the direction of applied strain (see Figure 4(d)). For ZZ PNTs, the values of these angles depend on the tube diameter. The value of the  $\alpha_o$  angle decreases as the ZZ tube diameter increases.

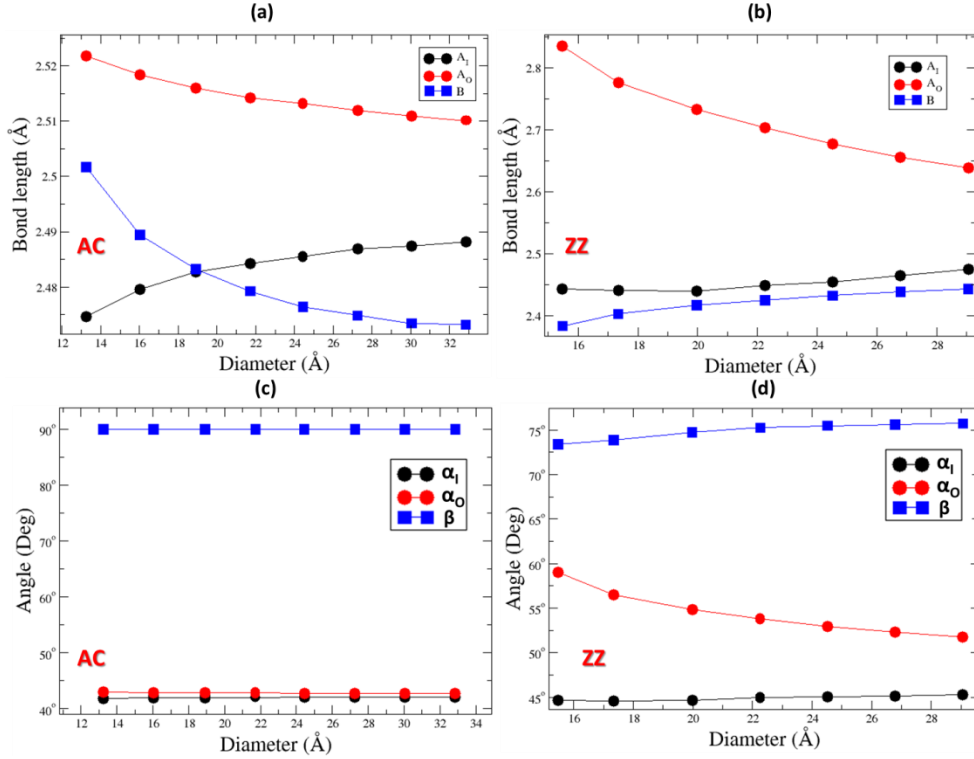


Figure 4: (a) Bond length of A<sub>1</sub> (black circles), A<sub>0</sub> (red circles) and B (blue squares) bonds of AC PNT are plotted vs nanotube diameter. (b) Bond length of A<sub>1</sub> (black circles), A<sub>0</sub> (red circles) and B (blue squares) bonds of ZZ PNT are plotted against nanotube diameter. (c) Angle between A<sub>1</sub> (black circles), A<sub>0</sub> (red circles) and B (blue squares) bonds and the stretching direction for AC PNT as a function of nanotube diameter. (d) Angle between A<sub>1</sub> (black circles), A<sub>0</sub> (red circles) and B (blue squares) bonds and the stretching direction for ZZ PNT as a function of nanotube diameter.

Due to the variations in the bond lengths and angles, the actual tube diameters and lengths are slightly different from the ideal ones obtained by rolling a phosphorene sheet, and the relaxation effects are more pronounced for PNTs with smaller diameters, and become negligible when the tube diameter is large, similar to carbon nanotubes [96], [97].

### 3.2 Flexural rigidity and Young's modulus

Next, we calculated the strain energy per atom associated with rolling up a phosphorene sheet in a tubular structure. The strain energy,  $E_s$ , was calculated as a difference between energy (per atom) of the tubular structure and phosphorene monolayer:  $E_s = \frac{E_{PNT}}{N} - E_{at}$ , where  $E_{PNT}$  is the total potential energy of the nanotube,  $N$  is the number of the nanotube atoms and  $E_{at}$  is the energy per atom in phosphorene monolayer. The strain energy as a function of tube diameter is shown in Figure 5(a). As can be seen from Figure 5(a), the strain energy per atom for ZZ PNTs is larger than that for AC PNTs. The difference is particularly noticeable for nanotubes with small diameters, and it decreases rapidly when the tube diameter increases. The lower strain energy per atom of AC PNTs indicates that they are energetically more favorable and stable than ZZ PNTs, in agreement with previous DFT calculations [55], [61].

As expected from the linear elasticity theory [101],[102],[103],[104], the strain energy varies as  $E_S = \frac{\delta}{D^2}$  with the tube diameter,  $D$ . Using data in Figure 5(a), we extracted the flexural (bending) rigidity,  $\delta$ . It was found that the flexural rigidity for AC PNT is  $\delta_{AC}=0.019$  (eV nm<sup>2</sup>/atom), which is almost three times smaller than that for ZZ PNT  $\delta_{ZZ}=0.071$  (eV nm<sup>2</sup>/atom).

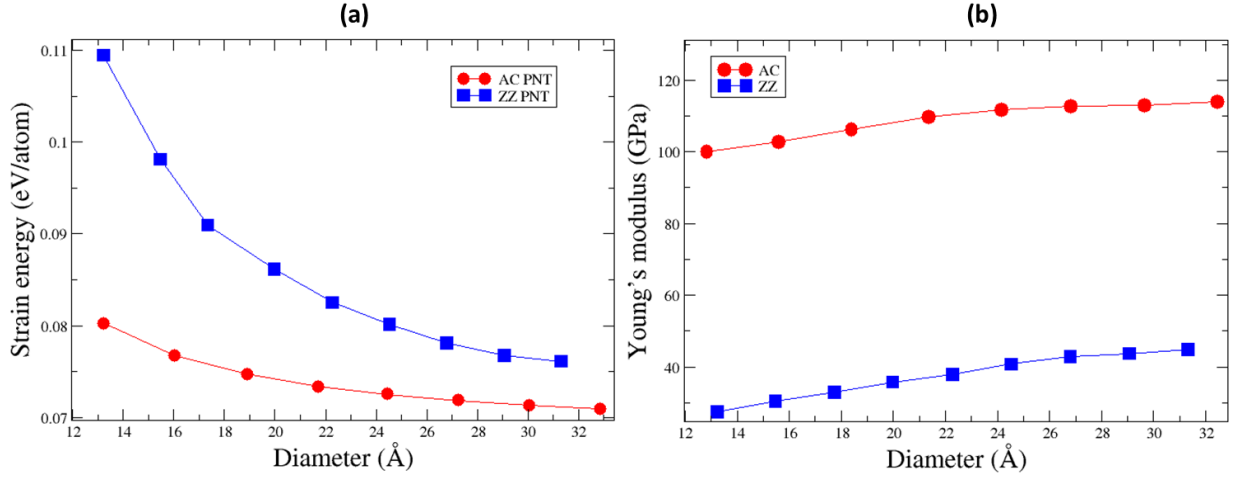


Figure 5: (a) Strain energy of AC (red circles) and ZZ (blue squares) PNTs as a function of tube diameter. (b) Young's modulus of AC (red circles) and ZZ (blue squares) PNTs as a function of tube diameter.

Additionally, we obtained the Young's modulus,  $Y$ , for AC and ZZ PNTs, which is related to the second derivative of the total potential energy,  $E_{PNT}$ , with respect to the strain (calculated at zero strain). More specifically,

$$Y = \frac{1}{V_0} \left( \frac{\partial^2 E_{PNT}}{\partial \varepsilon^2} \right)_{\varepsilon=0}$$

where  $V_0$  is the nanotube volume at zero strain. The second derivative of the total potential energy was calculated by subjecting PNTs to small uniaxial compressive and tensile strains ( $\varepsilon \leq 3\%$ ), and subsequent optimization of the atomic positions at each strain. The total potential energies for these small deformations were fitted to a second order polynomial, from which the second derivative at zero strain was found. The obtained Young's modulus for AC and ZZ PNTs as a function of tube diameter is shown in Figure 5(b). It is seen that the Young's modulus of AC PNTs is larger than that of ZZ PNTs in the examined range of the tube diameters. The value of Young's modulus for the ZZ PNT with the largest diameter is  $Y \approx 40$  GPa, while for the AC PNT of the similar diameter is  $Y \approx 115$  GPa, which is almost three times larger than that of the ZZ PNT. Another interesting observation is that the Young's modulus slightly depends on tube diameter. It gradually increases with the tube diameter and converges to a diameter-independent constant value (see Figure 5(b)). The effect of the tube diameter on the elastic properties of PNTs is only significant for small diameter PNTs ( $D \leq 20 \text{Å}$ , see Figure 5(b)). The similar effect of tube softening with decreasing diameter was also found for carbon and boron-nitride nanotubes with small diameters [96],[103],[105],[106],[107]. This minor reduction in the Young's modulus at small diameters can be

ascribed to the minor weakening of P-P bonds due to the tube curvature. As can be seen in Figure 4 (a, b), the P-P bond (namely, the  $A_i$  and  $A_o$  bonds for AC PNTs and the B-bonds for ZZ PNTs), stretched along the direction of applied tensile strain, are initially pre-compressed due to the tube curvature. Therefore, when the uniaxial tensile strain is applied, the length of these bonds first reverts to its equilibrium bulk value, and then starts to increase. Hence, the Young's modulus reduces as the tube diameter decreases.

### 3.3 Poisson's ratios

We also calculated the radial Poisson's ratio,  $\nu_D$ , which is defined as the ratio of the transverse contraction strain  $\frac{\Delta D}{D}$  to the longitudinal extension strain  $\frac{\Delta L}{L}$  of PNTs, and can be defined as:

$$\frac{\Delta D}{D} = -\nu_D \frac{\Delta L}{L},$$

where  $D$  is the tube diameter and  $L$  is the tube length. The Poisson's ratio for the tube thickness,  $\nu_t$ , was calculated in the same way by replacing the diameter  $D$  with the tube thickness,  $t$ , which is defined as the difference between the outer and inner tube radii. The Poisson's ratios  $\nu_D$  and  $\nu_t$  are both positive since the elongation of PNTs along the axial direction reduces the diameter and thickness (see Figure 6 and Figure 7). The diameter of AC and ZZ PNTs decreases in a different way with applied tensile strain. As can be seen from Figure 6 (a, b), AC PNTs contract in the transverse direction much more than ZZ PNTs. This noticeable distinction can be explained by the difference in the geometrical structure of PNTs. The puckered structure of AC PNTs (where the phosphorene puckers are aligned along the tube circumference) accounts for the substantial compressibility in the radial direction (see Figure 6 (a)). A pucker in phosphorene resembles a hinge, i.e. a jointed flexible device that allows the turning of a part on a stationary frame. At these puckers, the B-bonds, which are oriented along the radial direction and connect to adjacent  $A_i$  and  $A_o$  bonds (see Figure 3), can pivot around. Thus, the rotation of B-bonds, together with their minor contraction, leads to a considerable compression of AC PNTs in the radial direction. In ZZ PNTs, where the phosphorene puckers are aligned along the tube axis, the diameter reduction in the radial direction is due to the compression of the  $A_i$  and  $A_o$  bonds. Since the bond compression costs a significant amount of energy, the contraction in the transverse direction of ZZ PNTs is smaller than that of AC PNTs.

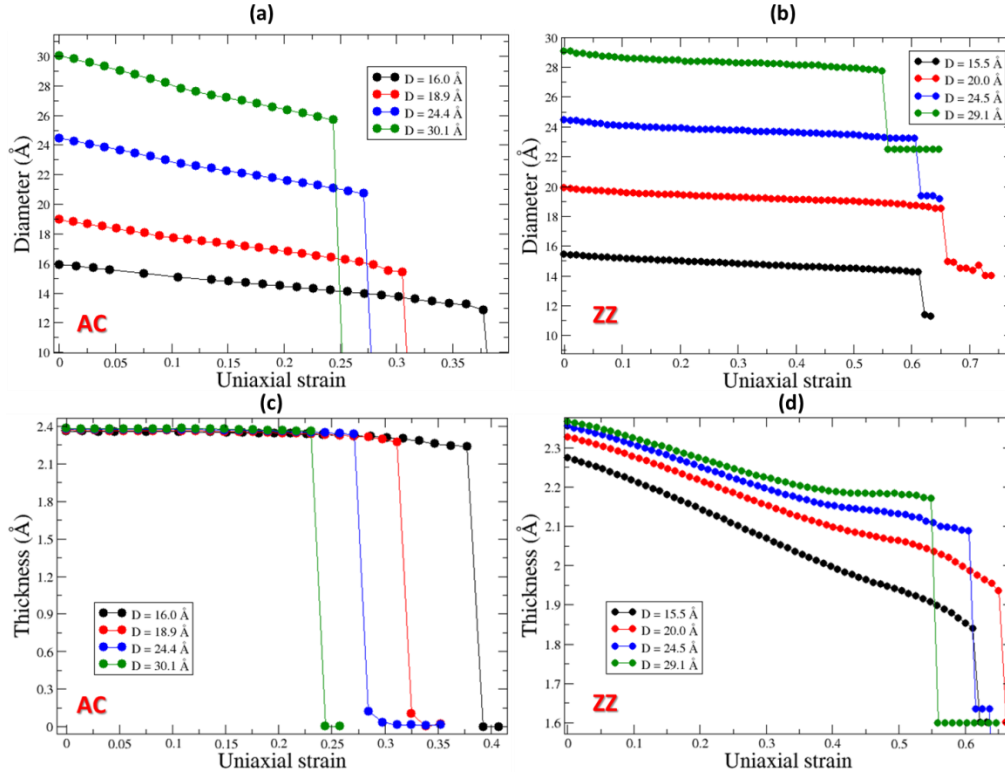


Figure 6: (a) Diameter of AC PNTs as a function of uniaxial tensile strain. Initial diameters (measured at zero strain) of AC PNTs are  $D=16.0$  Å (black circles),  $D=18.9$  Å (red circles),  $D=24.4$  Å (blue circles) and  $D=30.1$  Å (green circles), respectively. (b) Diameter of ZZ PNTs is plotted vs. applied uniaxial tensile strain. Initial diameters (measured at zero strain) are  $D=15.5$  Å (black circles),  $D=20.0$  Å (red circles),  $D=24.5$  Å (blue circles) and  $D=29.1$  Å (green circles). (c) Thickness of AC PNTs as a function of applied tensile strain. Initial diameters are  $D=16.0$  Å (black circles),  $D=18.9$  Å (red circles),  $D=24.4$  Å (blue circles) and  $D=30.1$  Å (green circles). (d) Thickness of ZZ PNTs as a function of applied tensile strain. Initial diameters are  $D=15.5$  Å (black circles),  $D=20.0$  Å (red circles),  $D=24.5$  Å (blue circles) and  $D=29.1$  Å (green circles).

The tube thickness changes with applied tensile strain in an opposite way. The thickness of AC PNTs with various diameters changes insignificantly with the applied tensile strain (see Figure 6(c)). On the other hand, the thickness of ZZ PNTs decreases abruptly with the applied tensile strain as shown in Figure 6(d). In addition, there is also an apparent dependence of the tube thickness on the tube diameter. As can be seen in Figure 6(d), the smaller is the ZZ PNT diameter, the larger is the decrease in its thickness.

We calculated both the radial (see Figure 7(a)) and thickness (see Figure 7(b)) Poisson's ratios as a function of diameter for AC and ZZ PNTs. As can be understood from Figure 7(a), the radial Poisson's ratio for AC PNTs ( $\nu_D = 0.47$ ) is almost seven times larger than that for ZZ PNTs ( $\nu_D = 0.07$ ). Similar to carbon nanotubes, the radial Poisson's ratio moderately depends on the tube diameter (a slight reduction for small radii) [103],[105],[96],[107]. The value of the radial Poisson's ratio converges to a constant at the large diameters. The Poisson's ratio for the tube thickness as a function of tube diameter is shown in Figure 7(b). Clearly, the behavior is opposite to the radial dependence, which can be explained by the tube geometry. The thickness Poisson's ratio for AC PNTs is a constant ( $\nu_t=0.11$ ), independent of tube diameter; while the thickness Poisson's ratio of ZZ PNTs decreases from  $\nu_t=0.25$  and gradually converges to  $\nu_t=0.21$  as the tube diameter increases.

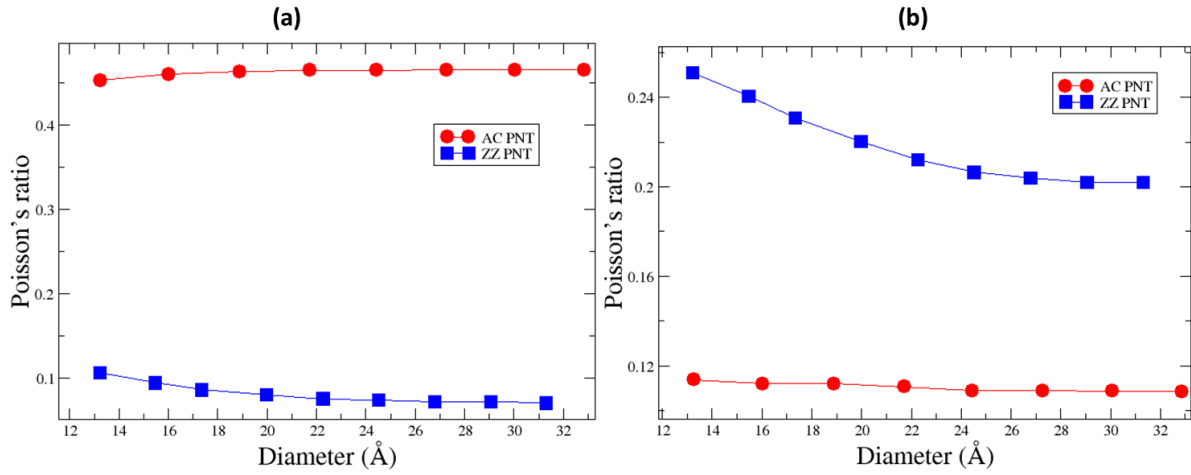


Figure 7: Poisson's ratio for contraction in the transverse direction of tube diameter (a) and thickness (b) of AC (red circles) and ZZ (blue squares) PNTs due to tensile strain applied in the longitudinal direction.

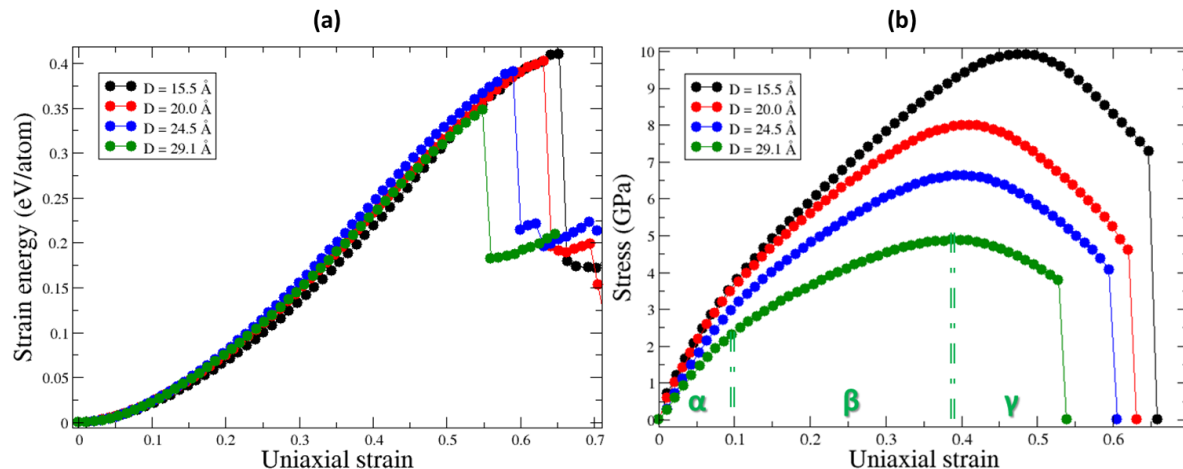
We summarize our calculated values for the elastic moduli, flexural rigidity and Poisson's ratios of PNTs in Table 1. Since the elastic moduli and Poisson's ratios only slightly or moderately depend on the tube diameter, we use the converged values for the large tube diameters.

Table 1: Elastic modulus, flexural rigidity and Poisson's ratios of phosphorene nanotubes

Nanotube type	Young's modulus (GPa)	Flexural rigidity (eV nm <sup>2</sup> /atom)	Poisson's ratio (radial)	Poisson's ratio (thickness)
AC	114.2	0.019	0.47	0.11
ZZ	49.2	0.071	0.07	0.21

### 3.4 ZZ PNTs: tensile deformation and failure pattern

In the following, we investigate the deformation and failure of ZZ PNTs at large strains. The tensile strain was step by step applied along the tube axis. The strain energy of ZZ PNTs, calculated with respect to the equilibrium nanotube configuration at zero strain, is shown in Figure 8(a). The strain energy is plotted for a selected set of ZZ PNTs with different diameters. In addition, we also calculated the stress as a function of tensile strain applied for the same set of ZZ PNTs (see Figure 8(b)).



**Figure 8:** (a) Strain energy (per atom) plotted vs. uniaxial tensile strain for ZZ PNTs of different diameters:  $D=15.5 \text{ \AA}$  (black circles),  $D=20.0 \text{ \AA}$  (red circles),  $D=24.5 \text{ \AA}$  (blue circles) and  $D=29.1 \text{ \AA}$  (green circles). (b) Stress-strain curves for ZZ PNTs of different diameters:  $D=15.5 \text{ \AA}$  (black circles),  $D=20.0 \text{ \AA}$  (red circles),  $D=24.5 \text{ \AA}$  (blue circles) and  $D=29.1 \text{ \AA}$  (green circles). Three phases of ZZ PNT deformation  $\alpha$ ,  $\beta$ , and  $\gamma$  are indicated.

As indicated in Figure 8(b), there are three characteristic phases (marked as  $\alpha$ ,  $\beta$ ,  $\gamma$ ) in the tensile deformation of ZZ PNTs. At a small strain ( $\epsilon \lesssim 0.1$ ), the linear elastic phase ( $\alpha$ -phase in Figure 8(b)) was detected; when the tensile strain surpassed  $\epsilon \approx 0.1$ , the bond rotation phase was observed ( $\beta$ -phase in Figure 8(b)), where the folded structure of phosphorene nanotubes was unfolded via the B-bond rotation. As a final point, when the tensile strain exceeded  $\epsilon \gtrsim 0.4$ , the direct B-bond stretching phase followed ( $\gamma$ -phase in Figure 8(b)), which was ended by B-bond breaking at the failure strain of  $\epsilon_{cr} \approx 0.6$ .

At the linear elastic phase, we found that the potential energy increases non-linearly as a quadratic function of applied tensile strain (see the  $\alpha$ -phase in Figure 8(b)), while the stress increases linearly. This phase completes when the uniaxial strain approaches  $\epsilon \approx 0.1$ . Similar to phosphorene nanoribbons [90], the end of the linear elastic phase is related to the puckered structure of phosphorene: each P-atom is tightly connected to its nearest neighboring atoms by strong covalent bonds. Moreover, it interacts with its next nearest neighbors situated in the neighboring phosphorene puckers (see Figure 1(a)). The pucker-pucker distance falls within the radius of inter-atomic interaction [90] at zero strain, however, upon tensile stretching, the distance between the two atoms from the adjacent puckers increases. This range of pucker-pucker inter-atomic interaction is exceeded at the strain  $\epsilon \approx 0.1$ . Therefore, above  $\epsilon \approx 0.1$ , the interaction between these pucker atoms turns out to be insignificantly small, and consequently, the linear elastic phase terminates.

Subsequently the elongation of ZZ PNTs is achieved via the rotation of B-bonds (see Figure 8(b)). The change in the bond length of B-bonds at the  $\beta$ -phase is negligible, as can be seen from Figure 9(a). The B-bond rotation causes the unfolding of the puckered structure of ZZ PNTs. The rotation angle, defined as an angle between a B-bond and the direction of applied strain is plotted in Figure 9 (b). The rotation angle decreases linearly with applied strain from its initial value  $\beta \approx 75^\circ$  to  $\beta \approx 40^\circ \sim 50^\circ$  at the failure strain, depending on the tube diameter (see Figure 9 (d)).

As soon as the applied strain goes beyond  $\epsilon \approx 0.4$ , the B-bond rotation phase is replaced by the B-bond stretching phase (see the  $\gamma$ -phase in Figure 8(b)), in which the B-bond length starts to increase steeply with applied tensile strain (see Figure 9 and Figure 10(b)). At the same time, the bond length of  $A_i$  and  $A_o$  bonds decreases. As soon as the critical tensile strain  $\epsilon_{cr} \approx 0.6$  is reached, the B-bonds begin to break along the entire length of the nanotube (see Figure 10(c)), releasing the accumulated strain energy. A P-P bond ruptures when its length exceeds the maximal bond length, which is about  $l_{max} = 2.9 \text{ \AA}$  [89], [90]. The pattern of the ruptured bonds at the critical failure strain for ZZ PNTs is shown in Figure 10(c). It should be noted that only a fraction of the B-bonds rupture at the critical strain. The bond length variation at the failure strain is indicated by the error bars in Figure 9(a, c).

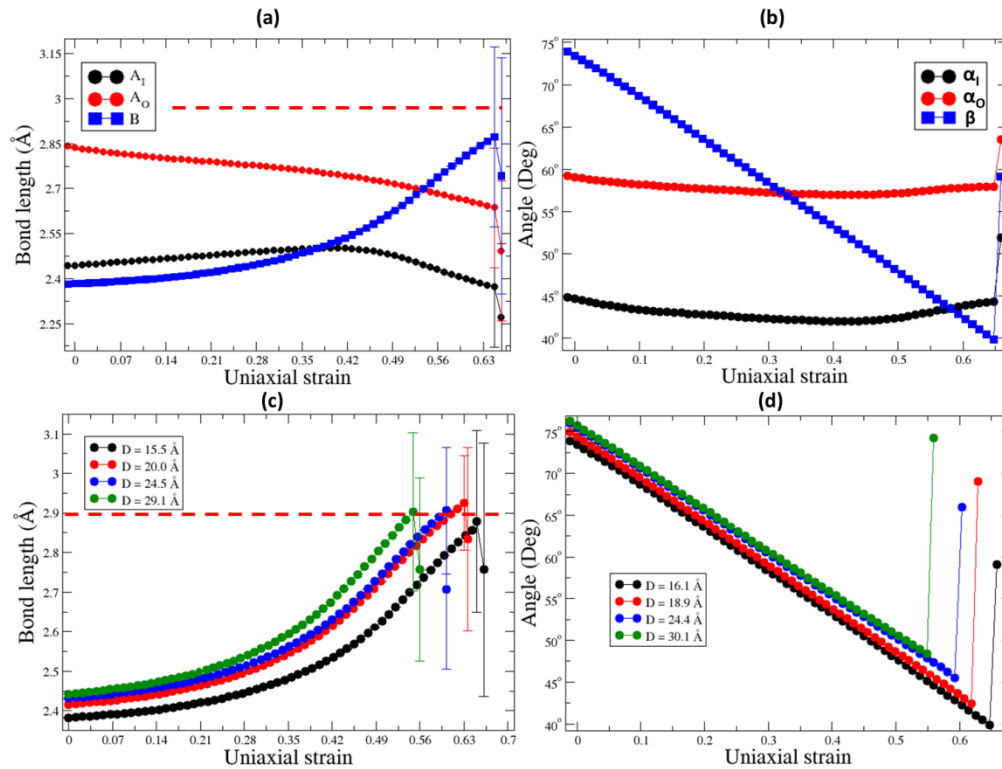


Figure 9: (a) Average bond length of  $A_i$  (black circles),  $A_o$  (red circles) and B (blue squares) bonds of ZZ PNT ( $D=24.5 \text{ \AA}$ ) as a function of applied tensile strain. Error bars indicate the bond length variation at the failure strain. The red dashed line specifies the maximally allowed bond length. (b) Average angles between the  $A_i$  (black circles),  $A_o$  (red circles) and B (blue squares) bonds and stretching direction for ZZ PNT ( $D=24.5 \text{ \AA}$ ) are plotted against applied tensile strain. (c) Average bond length of the B-bonds and (d) angle between B-bonds and stretching direction are plotted vs. applied tensile strain for ZZ PNTs with  $D=15.5 \text{ \AA}$  (black circles),  $D=20.0 \text{ \AA}$  (red circles),  $D=24.5 \text{ \AA}$  (blue circles) and  $D=29.1 \text{ \AA}$  (green circles). The red dashed line designates the maximally allowed bond length. Error bars indicate the bond length variation at the failure strain.

These three phases of deformation are universal for ZZ PNTs with different diameters. As shown in Figure 9(c, d), the B-bond rotation and elongation phases are the same for all ZZ PNTs with different diameters, although the particular values of tensile strain at which one phase is replaced by another phase and at which ZZ PNTs fail depend slightly on the tube diameter.

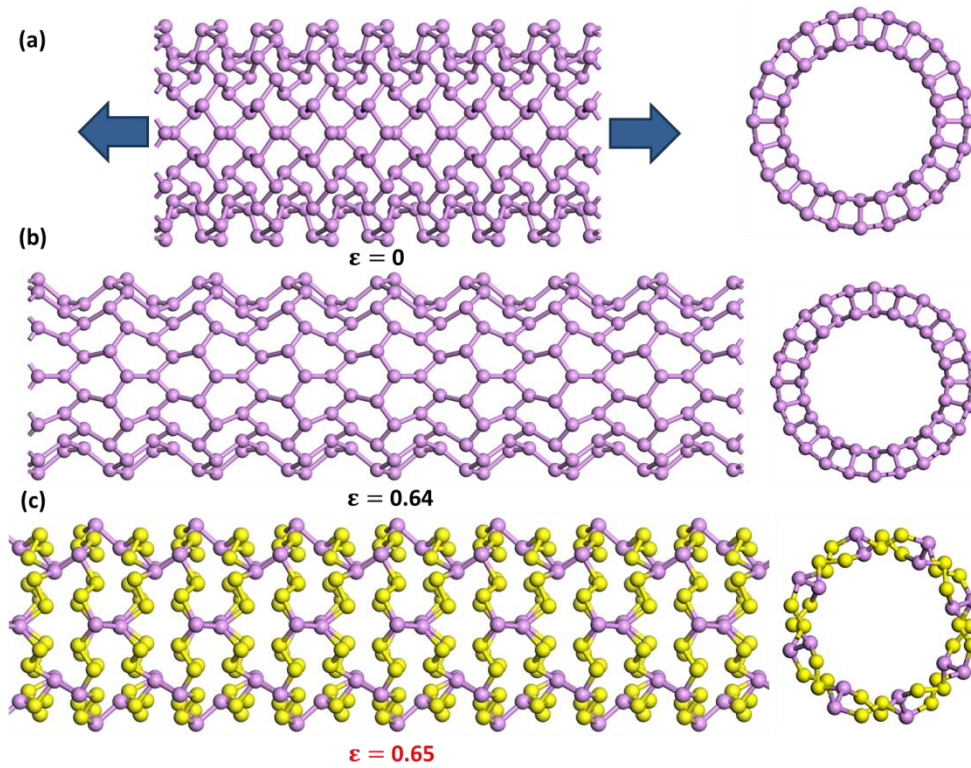


Figure 10: Deformation and failure of ZZ PNTs under applied uniaxial tensile strain (side and front views). Sequence of snapshots of ZZ PNT with  $D=24.5 \text{ \AA}$  at different strains: (a)  $\epsilon=0$  (reference configuration), (b)  $\epsilon=0.64$  (c), and  $\epsilon_{cr}=0.65$  (critical strain). P atoms that are connected by less than three P-P bonds are marked by yellow.

### 3.5 AC PNTs: tensile deformation and failure mechanism

Next, we studied the behavior of AC PNTs under uniaxial tensile strain and the results for the strain energy and stress are shown in Figure 11.

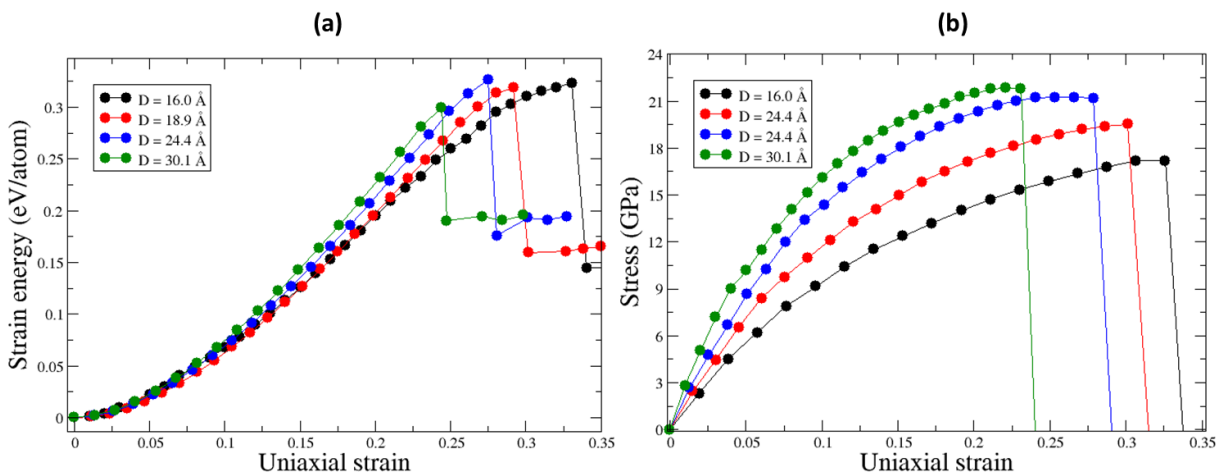


Figure 11: (a) Strain energy per atom as a function of applied uniaxial tensile strain for AC PNTs with different diameters:  $D=16.0 \text{ \AA}$  (black circles),  $D=18.9 \text{ \AA}$  (red circles),  $D=24.4 \text{ \AA}$  (blue circles) and  $D=30.1 \text{ \AA}$  (green circles). (b) Stress-strain curves of AC PNTs with different diameters:  $D=16.0 \text{ \AA}$  (black circles),  $D=18.9 \text{ \AA}$  (red circles),  $D=24.4 \text{ \AA}$  (blue circles) and  $D=30.1 \text{ \AA}$  (green circles).

The calculated stress-strain curves for AC PNTs reveal a very different characteristic: a rapid increase in the strain energy, which culminates at the failure of AC PNTs when the length of the strained bonds exceeds the maximally allowed limit. For AC PNTs, unlike to ZZ PNTs, the applied strain causes the direct straining of the  $A_i$  and  $A_o$  bonds from the outset (see Figure 12(a)). Their bond length increases as a linear function with the uniaxial strain regardless the tube diameter (see Figure 12 (c)). The orientation of these bonds also changes accordingly as they pivot to align along the direction of stretching. The change in the rotation angles  $\alpha_i$  and  $\alpha_o$  (see Figure 3(c)) is about  $\Delta\alpha_i=\Delta\alpha_o\approx 10^\circ$  (see Figure 12 (b, d)). The angles  $\alpha_i$  and  $\alpha_o$  decrease in the same way irrespective of the tube diameter as shown in Figure 12 (d). At the same time, the length of the B-bonds shortens, causing AC PNTs to contract in the radial direction. The orientation of the B-bonds, which are located at a right angle to the direction of applied strain, remains constant until the failure strain is reached (see Figure 12 (b)).

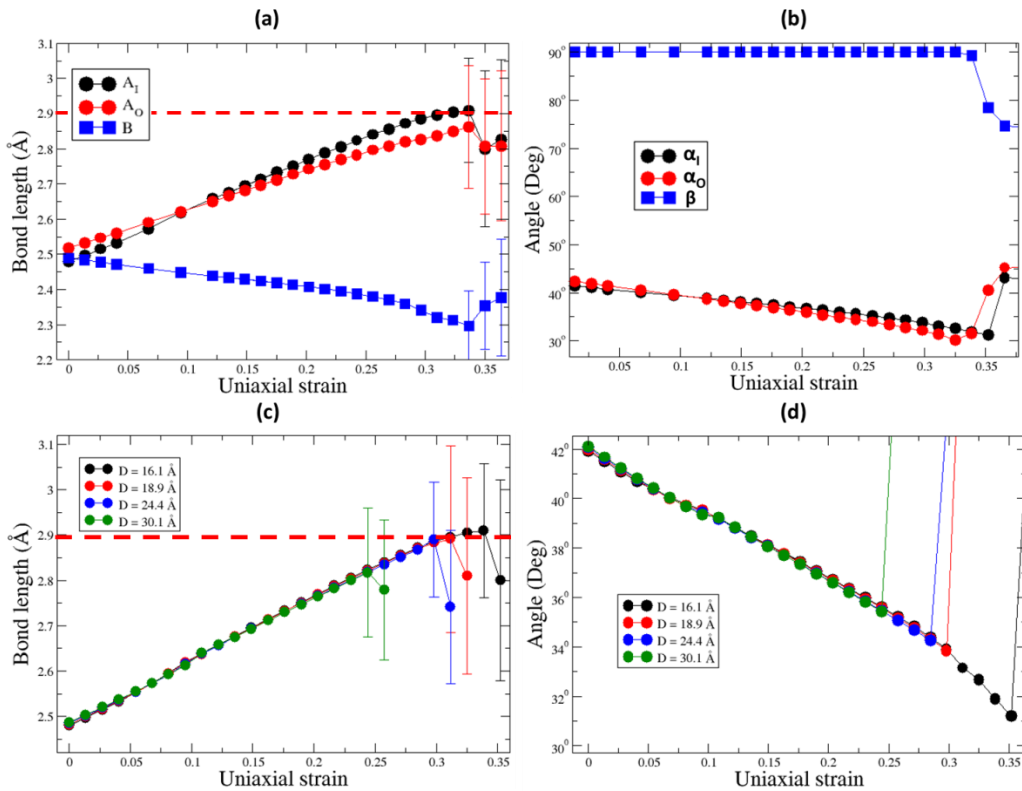


Figure 12: (a) Average bond length of  $A_i$  (black circles),  $A_o$  (red circles) and B (blue squares) bonds of AC PNT ( $D=18.95 \text{ \AA}$ ) as a function of applied tensile strain. Error bars indicate the bond length variation at the critical strain. The red dashed line specifies the maximally allowed bond length. (b) Average angle between  $A_i$  (black circles),  $A_o$  (red circles) and B (blue squares) bonds and the stretching direction for AC PNT ( $D=18.9 \text{ \AA}$ ) vs. applied tensile strain. (c) Average bond length of the B-bonds and (d) angle between B-bonds and stretching direction are plotted against the applied tensile strain for AC PNTs with  $D=16.1 \text{ \AA}$  (black circles),  $D=18.9 \text{ \AA}$  (red circles),  $D=24.4 \text{ \AA}$  (blue circles) and  $D=30.1 \text{ \AA}$  (green circles). The red dashed line specifies the maximally allowed bond length. Error bars indicate the bond length variation at the failure strain.

In order to comprehend the failure mechanism of AC PNTs, the AC PNT with diameter  $D=18.6 \text{ \AA}$  was examined. The snapshots for the failure process are shown in Figure 13. It is seen that near the failure strain, the  $A_i$  and  $A_o$  bonds are stretched to their limit (see Figure 13(b)), and at the critical strain  $\epsilon_{cr}\approx 0.31$ , a fraction of these strained bonds rupture. The substantial bond length variation at the critical

strain is indicated by error bars in Figure 12(a, c). The ruptured  $A_i$  and  $A_o$  bonds are uniformly distributed along the AC nanotubes. Note that due to the radial contraction of AC PNTs in the transverse direction, the distance between the neighboring puckers, which are located along the nanotube circumference, decreases substantially. As a result, at the critical strain, the adjacent puckers are drawn close enough to form bonds between the atoms located in the inner tube shell. The bond rupture at the failure strain is accompanied by the formation of the new bonds and irreversible rearrangement of the old bonds between the atoms of the inner and outer tube shells (see Figure 13(c)).

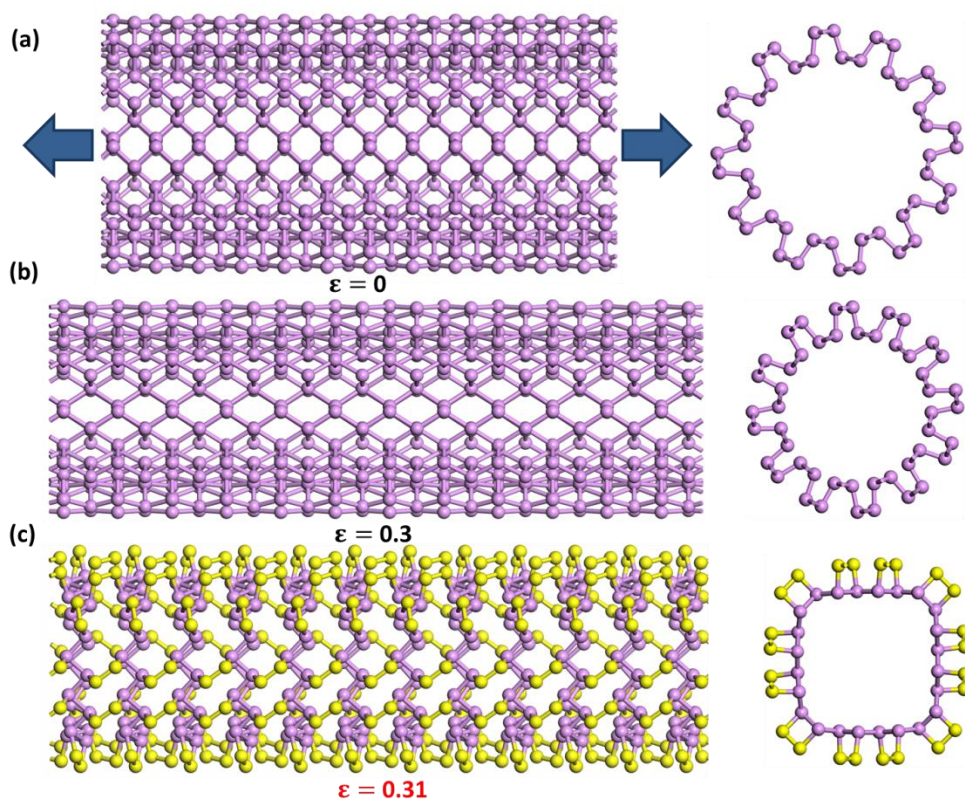


Figure 13: Deformation and failure of AC PNTs subjected to uniaxial tensile strain (side and front views). (a - b) Sequence of snapshots of AC PNT with  $D = 18.6 \text{ \AA}$  at different tensile strains: (a)  $\epsilon = 0$  (reference configuration), (b)  $\epsilon = 0.3$ , and (c)  $\epsilon = 0.31$  (critical strain).

### 3.6 Critical strain and stress

Our simulations indicate that the failure strain for AC PNTs is in the range from  $\epsilon \approx 0.25$  to  $\epsilon \approx 0.4$ , and for ZZ PNTs it is between  $\epsilon \approx 0.55$  and  $\epsilon \approx 0.66$  (see Figure 14). Thus, the failure strain of ZZ PNTs is almost two times larger than that of AC PNTs. In ZZ PNTs, the applied strain causes the rotation and straining of the B-bonds connecting P atoms between the adjacent tube shells, while in AC PNTs, the  $A_i$  and  $A_o$  bonds linking atoms within the inner and outer tube shells are the most strained. Evidently, the noticeable variances in the mechanical properties and failure behavior of the ZZ and AC PNTs originate from the

difference in the nanotube geometry. From the obtained stress-strain curves for ZZ PNTs (see Figure 8(b)) and AC PNTs (see Figure 8(b)), we calculated the failure strain and failure stress as a function of nanotube diameter, which are shown in Figure 14. The failure strain as a function of tube diameter for AC (red circles) and ZZ (blue squares) PNTs is plotted in Figure 14(a). For AC PNTs, the failure strain decreases steadily from  $\epsilon_{cr} \approx 0.4$  to  $\epsilon_{cr} \approx 0.25$  with the tube diameter within the range examined in our DFTB simulations. This decrease in the critical strain with the tube diameter is related to the fact that AC PNTs with smaller diameters are partially reinforced by an increase in the magnitude of interactions between the adjacent puckers. This is because the distance between the adjacent puckers is shorter for AC PNTs with smaller diameters due to their contraction in the transverse (radial) direction under applied axial strain. The increase in the magnitude of adjacent pucker-pucker interactions allows AC PNTs to accommodate larger stretching. Moreover, the applied tensile strain mostly stretches the  $A_i$  and  $A_o$  bonds oriented along the direction of the axial strain (see Figure 12(a)). Since at zero strain, the length of the  $A_i$ -bonds is shorter for AC nanotubes with the smaller diameter (see Figure 4(a)), as a result, a larger tensile strain is needed to reach the critical failure strain, causing the bond fracture.

For ZZ PNTs, the critical strain also decreases with the tube diameter from  $\epsilon_{cr} \approx 0.66$  to  $\epsilon_{cr} \approx 0.55$  (see Figure 14(a), blue squares). In contrast to AC PNTs, tensile strain applied to ZZ PNTs predominantly elongates the B-bonds, which are in parallel with the tube axis, and to a less extent, the  $A_i$  and  $A_o$  bonds as shown in Figure 9. Akin to AC PNTs, the bond length of these bonds shortens as the tube diameter decreases (see Figure 4(b)). Therefore, ZZ PNTs with smaller diameters can be elongated considerably longer than ZZ PNTs with larger diameters before their stretched B-bonds reach the maximally allowed bond length limit.

The failure stress as a function of PNT diameter is shown in Figure 14(b). For both AC and ZZ nanotube geometries, the failure stress decreases as the tube diameter increases. The maximal failure stress for AC PNTs is  $\sigma_{cr} \approx 21$  GPa, while for ZZ PNTs, it is  $\sigma_{cr} \approx 9$  GPa, which is approximately half that of the AC PNT value. The minimal value for the failure stress of AC PNTs is  $\sigma_{cr} \approx 13$  GPa, while for ZZ PNTs, it is  $\sigma_{cr} \approx 4$  GPa, which is approximately three times lower than that of the AC PNT value.

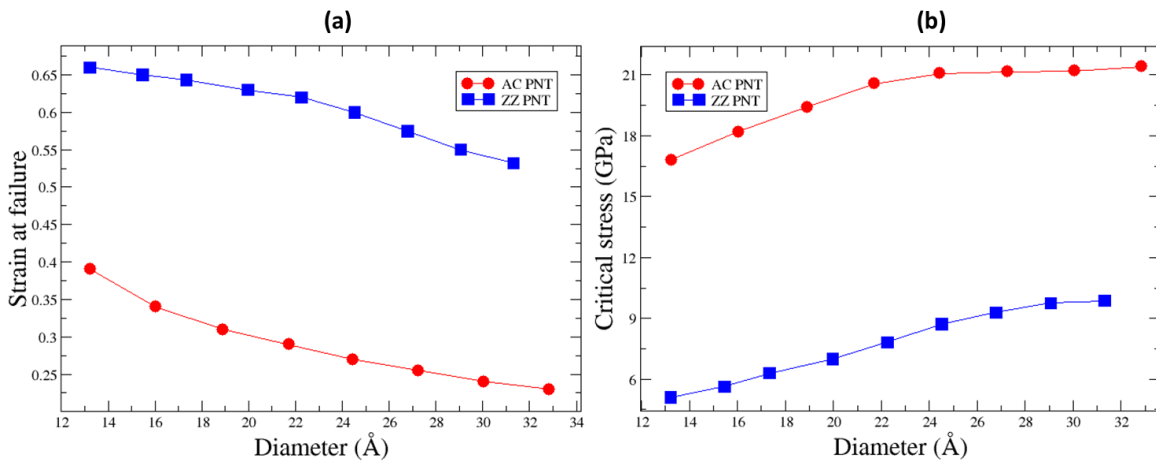


Figure 14: (a) Strain at failure (critical strain) plotted against diameter of AC (red circles) and ZZ (blue circles) PNTs; (b) critical (failure) stress plotted vs. diameter of AC (red circles) and ZZ (blue circles) PNTs.

## 4. Conclusions

Applying DFTB method, we have examined the elastic properties, deformation and failure of AC and ZZ PNTs subjected to uniaxial tensile strain. Before the tensile strain has been used, the geometry of the phosphorene nanotubes, constructed by rolling up a sheet of phosphorene, was optimized. The resulting optimization reveals the alteration of the bond length and angles of PNTs. The curvature effects on the geometric parameters and energetics of PNTs have been examined. The obtained energies, which are inversely proportional to the square of tube diameter, are in good agreement with the classical elasticity theory. In addition, we have also calculated the Young modulus, flexural rigidity and Poisson's ratios as a function of tube diameter. It is found that these quantities are relatively insensitive to the tube diameter.

We have revealed and analyzed three phases of the deformation of ZZ PNTs subjected to uniaxial tensile strain. The initial phase is the linear elastic phase at low strain ( $\epsilon \lesssim 0.1$ ), which is associated with the interaction of the nearby puckers. The next phase is the bond rotation phase ( $0.1 \lesssim \epsilon \lesssim 0.4$ ), where the folded configuration of the ZZ PNTs is gradually unfolded. This flattening is caused by the rotation of the B-bonds, connecting the P-atoms between the adjacent tube shells. The change in the length of the B-bonds is insignificant at this phase. The third phase is the bond straining phase ( $\epsilon \gtrsim 0.4$ ), where the bond length of the B-bonds grows steeply and finally exceeds the allowable bond length maximum. The failure of ZZ PNTs is resulted from the B-bonds fracture at  $\epsilon_{cr} \gtrsim 0.6$ .

For AC PNTs, the applied tensile strain from the outset results in the stretching of the  $A_i$  and  $A_o$  bonds, connecting the P-atoms within the inner and outer tube shells. These bonds fracture at the failure strain  $\epsilon_{cr} \gtrsim 0.35$ , triggering the breakup of AC PNTs. The dissimilarity in the failure mechanisms of AC and ZZ PNTs is due to the dissimilarity in their geometry. In ZZ PNTs, the B-bonds are the most strained bonds under the applied strain and first to break. By contrast, the  $A_i$  and  $A_o$  bonds are the most stretched ones in AC PNTs. A substantial fraction of these bonds fractures concurrently at the failure strain.

For both AC and ZZ PNTs, their failure strain and failure stress are sensitive, while the Young's modulus, flexural rigidity, radial Poisson's ratio and thickness Poisson's ratio are relatively insensitive to the tube diameter. More specifically, for AC PNTs, the failure strain reduces from  $\epsilon_{cr} \approx 0.40$  to  $\epsilon_{cr} \approx 0.25$  while the failure stress rises from  $\sigma_{cr} \approx 13$  GPa to  $\sigma_{cr} \approx 21$  GPa when the tube diameter increases from  $D=13.3$  Å to  $D=32.8$  Å; for ZZ PNTs, the failure strain diminishes from  $\epsilon_{cr} \approx 0.66$  to  $\epsilon_{cr} \approx 0.55$  while the failure stress increases from  $\sigma_{cr} \approx 4$  GPa to  $\sigma_{cr} \approx 9$  GPa when the tube diameter increases from  $D=13.2$  Å to  $D=31.1$  Å. The Young's modulus, flexural rigidity, radial and thickness Poisson ratios are  $Y=114.2$  GPa,  $\delta=0.019$  eV·nm<sup>2</sup>,  $\nu_D = 0.47$  and  $\nu_t = 0.11$  for AC PNTs, and  $Y=49.2$  GPa,  $\delta=0.071$  eV·nm<sup>2</sup>,  $\nu_D = 0.07$  and  $\nu_t = 0.21$  for ZZ PNTs, respectively.

Due to their many fascinating properties, PNTs may find various novel applications in electronic, photonic, sensing and energy conversion et al. It is expected that the present findings provide suitable guidelines for the designs and applications of PNTs as building blocks in nano-devices.

## 5. Acknowledgements

The authors want to express their gratitude for the financial funding from A\*STAR, Singapore and the usage of supercomputing services at ACRC, Singapore.

- [1] F. Xia, H. Wang, and Y. Jia, "Rediscovering black phosphorus as an anisotropic layered material for optoelectronics and electronics.," *Nat. Commun.*, vol. 5, p. 4458, Jan. 2014.
- [2] X. Ling, H. Wang, S. Huang, F. Xia, and M. S. Dresselhaus, "The renaissance of black phosphorus," *Proc. Natl. Acad. Sci.*, vol. 112, no. 15, p. 201416581, Mar. 2015.
- [3] J. Na, Y. T. Lee, J. A. Lim, D. K. Hwang, G. Kim, W. K. Choi, Y. Song, I. Control, F. Convergence, S. Korea, E. Engineering, and S. Korea, "Few-Layer Black Phosphorus Field-Effect Transistors with," no. 11, pp. 11753–11762, 2014.
- [4] J. R. Brent, N. Savjani, E. A. Lewis, S. J. Haigh, D. J. Lewis, and P. O'Brien, "Production of few-layer phosphorene by liquid exfoliation of black phosphorus.," *Chem. Commun. (Camb).*, vol. 50, no. 87, pp. 13338–41, Nov. 2014.
- [5] F. Xia, H. Wang, and Y. Jia, "Rediscovering black phosphorus as an anisotropic layered material for optoelectronics and electronics.," *Nat. Commun.*, vol. 5, p. 4458, Jan. 2014.
- [6] A. Castellanos-Gomez, L. Vicarelli, E. Prada, J. O. Island, K. L. Narasimha-Acharya, S. I. Blanter, D. J. Groenendijk, M. Buscema, G. a. Steele, J. V. Alvarez, H. W. Zandbergen, J. J. Palacios, and H. S. J. van der Zant, "Isolation and characterization of few-layer black phosphorus," *2D Mater.*, vol. 1, no. 2, p. 025001, 2014.
- [7] W. Lu, H. Nan, J. Hong, Y. Chen, C. Zhu, Z. Liang, X. Ma, Z. Ni, C. Jin, and Z. Zhang, "Plasma-assisted fabrication of monolayer phosphorene and its Raman characterization," *Nano Res.*, vol. 7, no. 6, pp. 853–859, May 2014.
- [8] K. S. S. K. S. Novoselov, A. K. A. K. Geim, S. V. S. V Morozov, D. Jiang, Y. Zhang, S. V. V Dubonos, I. V. V Grigorieva, and A. A. A. Firsov, "Electric field effect in atomically thin carbon films.," *Science (80-. )*, vol. 306, no. 5696, pp. 666–669, Oct. 2004.
- [9] A. K. Geim and K. S. Novoselov, "The rise of graphene.," *Nat. Mater.*, vol. 6, no. 3, pp. 183–191, 2007.
- [10] K. Watanabe, T. Taniguchi, and H. Kanda, "Direct-bandgap properties and evidence for ultraviolet lasing of hexagonal boron nitride single crystal.," *Nat. Mater.*, vol. 3, no. 6, pp. 404–9, Jun. 2004.

- [11] L. Song, L. Ci, H. Lu, P. B. Sorokin, C. Jin, J. Ni, A. G. Kvashnin, D. G. Kvashnin, J. Lou, B. I. Yakobson, and P. M. Ajayan, "Large scale growth and characterization of atomic hexagonal boron nitride layers," *Nano Lett.*, vol. 10, pp. 3209–3215, 2010.
- [12] K. K. Kim, A. Hsu, X. Jia, S. M. Kim, Y. Shi, M. Dresselhaus, T. Palacios, and J. Kong, "Synthesis and characterization of hexagonal boron nitride film as a dielectric layer for graphene devices," *ACS Nano*, vol. 6, pp. 8583–8590, 2012.
- [13] V. K. Sangwan, H. N. Arnold, D. Jariwala, T. J. Marks, L. J. Lauhon, and M. C. Hersam, "Low-frequency electronic noise in single-layer MoS<sub>2</sub> transistors," *Nano Lett.*, vol. 13, pp. 4351–4355, 2013.
- [14] V. Sorkin, H. Pan, H. Shi, S. Y. Quek, and Y. W. Zhang, "Nanoscale Transition Metal Dichalcogenides: Structures, Properties, and Applications," *Crit. Rev. Solid State Mater. Sci.*, vol. 39, pp. 319–367, 2014.
- [15] Q. H. Wang, K. Kalantar-Zadeh, A. Kis, J. N. Coleman, and M. S. Strano, "Electronics and optoelectronics of two-dimensional transition metal dichalcogenides," *Nat. Nanotechnol.*, vol. 7, pp. 699–712, 2012.
- [16] M. Chhowalla, H. S. Shin, G. Eda, L.-J. Li, K. P. Loh, and H. Zhang, "The chemistry of two-dimensional layered transition metal dichalcogenide nanosheets," *Nat. Chem.*, vol. 5, pp. 263–75, 2013.
- [17] M. Buscema, D. J. Groenendijk, S. I. Blanter, G. A. Steele, H. S. J. Van Der Zant, and A. Castellanos-Gomez, "Fast and broadband photoresponse of few-layer black phosphorus field-effect transistors," *Nano Lett.*, vol. 14, pp. 3347–3352, 2014.
- [18] Y. Du, H. Liu, Y. Deng, and P. D. Ye, "Device perspective for black phosphorus field-effect transistors: contact resistance, ambipolar behavior, and scaling," *ACS Nano*, vol. 8, no. 10, pp. 10035–42, Oct. 2014.
- [19] S. Das, W. Zhang, M. Demarteau, A. Hoffmann, M. Dubey, and A. Roelofs, "Tunable transport gap in phosphorene," *Nano Lett.*, vol. 14, no. 10, pp. 5733–9, Oct. 2014.
- [20] L. Li, Y. Yu, G. J. Ye, Q. Ge, X. Ou, H. Wu, D. Feng, X. H. Chen, and Y. Zhang, "Black phosphorus field-effect transistors," *Nat. Nanotechnol.*, vol. 9, pp. 372–7, 2014.
- [21] Y. Cai, G. Zhang, and Y.-W. Zhang, "Layer-dependent Band Alignment and Work Function of Few-Layer Phosphorene," *Sci. Rep.*, vol. 4, p. 6677, 2014.
- [22] W. Zhu, M. N. Yogeesh, S. Yang, S. H. Aldave, J. Kim, S. S. Sonde, L. Tao, N. Lu, and D. Akinwande, "Flexible Black Phosphorus Ambipolar Transistors, Circuits and AM Demodulator," *Nano Lett.*, vol. 15, pp. 1883–1890, Feb. 2015.
- [23] S. P. Koenig, R. a. Doganov, H. Schmidt, a. H. Castro Neto, and B. Özyilmaz, "Electric field effect in ultrathin black phosphorus," *Appl. Phys. Lett.*, vol. 104, p. 103106, 2014.

- [24] X. Han, H. Morgan Stewart, S. a. Shevlin, C. R. a. Catlow, and Z. X. Guo, "Strain and orientation modulated bandgaps and effective masses of phosphorene nanoribbons," *Nano Lett.*, vol. 14, pp. 4607–4614, 2014.
- [25] B. Sa, Y.-L. Li, J. Qi, R. Ahuja, and Z. Sun, "Strain Engineering for Phosphorene: The Potential Application as a Photocatalyst," *J. Phys. Chem. C*, vol. 118, no. 46, pp. 26560–26568, Nov. 2014.
- [26] H. Liu, A. T. Neal, Z. Zhu, Z. Luo, X. Xu, D. Tománek, and P. D. Ye, "Phosphorene: An unexplored 2D semiconductor with a high hole mobility," *ACS Nano*, vol. 8, pp. 4033–4041, 2014.
- [27] A. S. Rodin, A. Carvalho, and A. H. Castro Neto, "Strain-induced gap modification in black phosphorus," *Phys. Rev. Lett.*, vol. 112, p. 176801, 2014.
- [28] X. Peng, Q. Wei, and A. Copple, "Strain-engineered direct-indirect band gap transition and its mechanism in two-dimensional phosphorene," *Phys. Rev. B*, vol. 90, no. 8, p. 085402, Aug. 2014.
- [29] R. Fei and L. Yang, "Strain-engineering the anisotropic electrical conductance of few-layer black phosphorus," *Nano Lett.*, vol. 14, pp. 2884–2889, 2014.
- [30] J. Qiao, X. Kong, Z.-X. Hu, F. Yang, and W. Ji, "High-mobility transport anisotropy and linear dichroism in few-layer black phosphorus," *Nat. Commun.*, vol. 5, p. 4475, 2014.
- [31] Y. Li, S. Yang, and J. Li, "Modulation of the Electronic Properties of Ultrathin Black Phosphorus by Strain and Electrical Field," *J. Phys. Chem. C*, vol. 118, no. 41, pp. 23970–23976, Oct. 2014.
- [32] H. Morgan Stewart, S. a. Shevlin, C. R. a. Catlow, and Z. X. Guo, "Compressive Straining of Bilayer Phosphorene Leads to Extraordinary Electron Mobility at a New Conduction Band Edge," *Nano Lett.*, vol. 15, pp. 2006–2010, 2015.
- [33] Z.-Y. Ong, Y. Cai, G. Zhang, and Y.-W. Zhang, "Strong Thermal Transport Anisotropy and Strain Modulation in Single-Layer Phosphorene," *J. Phys. Chem. C*, vol. 118, no. 43, pp. 25272–25277, Oct. 2014.
- [34] Q. Wei and X. Peng, "Superior mechanical flexibility of phosphorene and few-layer black phosphorus," *Appl. Phys. Lett.*, vol. 104, no. 25, p. 251915, Jun. 2014.
- [35] J.-W. Jiang and H. S. Park, "Mechanical properties of single-layer black phosphorus," *J. Phys. D. Appl. Phys.*, vol. 47, no. 38, p. 385304, Sep. 2014.
- [36] T. Hu, Y. Han, and J. Dong, "Mechanical and electronic properties of monolayer and bilayer phosphorene under uniaxial and isotropic strains," *Nanotechnology*, vol. 25, no. 45, p. 455703, Nov. 2014.
- [37] D. Çakır, H. Sahin, and F. M. Peeters, "Tuning of the electronic and optical properties of single-layer black phosphorus by strain," *Phys. Rev. B*, vol. 90, no. 20, p. 205421, Nov. 2014.

- [38] M. Elahi, K. Khaliji, S. M. Tabatabaei, M. Pourfath, and R. Asgari, "Modulation of electronic and mechanical properties of phosphorene through strain," p. 8, Jul. 2014.
- [39] E. S. Reich, "Phosphorene excites materials scientists.," *Nature*, vol. 506, no. 7486, p. 19, Feb. 2014.
- [40] T. Low, M. Engel, M. Steiner, and P. Avouris, "Origin of photoresponse in black phosphorus phototransistors," *Phys. Rev. B*, vol. 90, no. 8, p. 081408, Aug. 2014.
- [41] L. Kou, T. Frauenheim, and C. Chen, "Phosphorene as a superior gas sensor: Selective adsorption and distinct  $i - V$  response," *J. Phys. Chem. Lett.*, vol. 5, pp. 2675–2681, 2014.
- [42] Y. Cai, Q. Ke, G. Zhang, and Y.-W. Zhang, "Energetics, Charge Transfer, and Magnetism of Small Molecules Physisorbed on Phosphorene," *J. Phys. Chem. C*, vol. 119, no. 6, pp. 3102–3110, Jan. 2015.
- [43] Y. Jing, Q. Tang, P. He, Z. Zhou, and P. Shen, "Small molecules make big differences: molecular doping effects on electronic and optical properties of phosphorene.," *Nanotechnology*, vol. 26, no. 9, p. 095201, Mar. 2015.
- [44] E. S. Information, V. V Kulish, O. I. Malyi, C. Persson, and P. Wu, "Adsorption of metal adatoms on single-layer phosphorene.," *Phys. Chem. Chem. Phys.*, vol. 17, no. 2, pp. 992–1000, Dec. 2014.
- [45] H. Y. Lv, W. J. Lu, D. F. Shao, and Y. P. Sun, "Large thermoelectric power factors in black phosphorus and phosphorene," vol. arXiv, p. 1404.5171, 2014.
- [46] R. Fei, A. Faghaninia, R. Soklaski, J.-A. Yan, C. Lo, and L. Yang, "Enhanced thermoelectric efficiency via orthogonal electrical and thermal conductances in phosphorene.," *Nano Lett.*, vol. 14, no. 11, pp. 6393–6399, Nov. 2014.
- [47] J. Zhang, H. J. Liu, L. Cheng, J. Wei, J. H. Liang, D. D. Fan, J. Shi, X. F. Tang, and Q. J. Zhang, "Phosphorene nanoribbon as a promising candidate for thermoelectric applications.," *Sci. Rep.*, vol. 4, pp. 4–10, Jan. 2014.
- [48] R. Zhang, B. Li, and J. Yang, "A First-Principles Study on Electron Donor and Acceptor Molecules Adsorbed on Phosphorene," *J. Phys. Chem. C*, vol. 119, no. 5, pp. 2871–2878, Jan. 2015.
- [49] S. Zhao, W. Kang, and J. Xue, "The potential application of phosphorene as an anode material in Li-ion batteries," *J. Mater. Chem. A*, vol. 2, no. 44, pp. 19046–19052, Sep. 2014.
- [50] W. Li, Y. Yang, G. Zhang, and Y.-W. Zhang, "Ultrafast and Directional Diffusion of Lithium in Phosphorene for High-Performance Lithium-Ion Battery," *Nano Lett.*, vol. 15, no. 3, pp. 1691–1697, 2015.
- [51] M. Buscema, D. J. Groenendijk, G. A. Steele, H. S. J. van der Zant, and A. Castellanos-Gomez, "Photovoltaic effect in few-layer black phosphorus PN junctions defined by local electrostatic gating.," *Nat. Commun.*, vol. 5, p. 4651, Jan. 2014.

- [52] Y. Deng, Z. Luo, N. J. Conrad, H. Liu, Y. Gong, S. Najmaei, P. M. Ajayan, J. Lou, X. Xu, and P. D. Ye, "Black phosphorus-monolayer MoS<sub>2</sub> van der Waals heterojunction p-n diode.," *ACS Nano*, vol. 8, no. 8, p. 37, Aug. 2014.
- [53] A. K. Geim and I. V Grigorieva, "Van der Waals heterostructures.," *Nature*, vol. 499, no. 7459, pp. 419–25, Jul. 2013.
- [54] J. Dai and X. C. Zeng, "Bilayer phosphorene: Effect of stacking order on bandgap and its potential applications in thin-film solar cells," *J. Phys. Chem. Lett.*, vol. 5, pp. 1289–1293, 2014.
- [55] H. Guo, N. Lu, J. Dai, X. Wu, and X. C. Zeng, "Phosphorene Nanoribbons, Phosphorus Nanotubes, and van der Waals Multilayers," *J. Phys. Chem. C*, vol. 118, pp. 14051–14059, 2014.
- [56] E. Taghizadeh Sisakht, M. H. Zare, and F. Fazileh, "Scaling laws of band gaps of phosphorene nanoribbons: A tight-binding calculation," *Phys. Rev. B*, vol. 91, no. February, p. 085409, 2015.
- [57] Q. Wu, L. Shen, M. Yang, Z. Huang, and Y. P. Feng, "Band Gaps and Giant Stark Effect in Nonchiral Phosphorene Nanoribbons.," vol. arXiv, p. 1405.3077, May 2014.
- [58] Q. Yao, C. Huang, Y. Yuan, Y. Liu, S. Liu, K. Deng, and E. Kan, "Theoretical Prediction of Phosphorene and Nanoribbons As Fast-Charging Li Ion Battery Anode Materials," *J. Phys. Chem. C*, vol. 119, pp. 6923–6928, 2015.
- [59] V. V Kulish, O. I. Malyi, C. Persson, and P. Wu, "Evaluation of Phosphorene as Anode Material for Na-ion Batteries from First Principles," vol. arXiv, p. 1501.02425, 2015.
- [60] A. Carvalho, A. S. Rodin, A. H. Castro Neto, and A. H. C. Neto, "Phosphorene nanoribbons," *Cornell Univ. Libr.*, vol. 108, no. 4, pp. 1–8, Nov. 2014.
- [61] G. Seifert and E. Hernández, "Theoretical prediction of phosphorus nanotubes," *Chemical Physics Letters*, vol. 318. pp. 355–360, 2000.
- [62] J. Guan, Z. Zhu, D. T. Physics, E. Lansing, and U. States, "Tiling Phosphorene ´," no. 12, pp. 12763–12768, 2014.
- [63] C. N. R. Rao, R. Seshadri, A. Govindaraj, and R. Sen, "Fullerenes, nanotubes, onions and related carbon structures," *Materials Science and Engineering: R: Reports*, vol. 15. pp. 209–262, 1995.
- [64] P. F. J. Harris, *Carbon nanotubes and related structures (1st ed.)*. Cambridge University Press, 2002.
- [65] T. W. Odom, J.-L. Huang, P. Kim, and C. M. Lieber, "Atomic structure and electronic properties of single-walled carbon nanotubes," *Nature*, vol. 391, pp. 62–64, 1998.
- [66] L. Huang, B. Wu, G. Yu, and Y. Liu, "Graphene: learning from carbon nanotubes," *Journal of Materials Chemistry*, vol. 21. p. 919, 2011.

- [67] M. Nardelli, B. Yakobson, and J. Bernholc, "Brittle and Ductile Behavior in Carbon Nanotubes," *Phys. Rev. Lett.*, vol. 81, no. 21, pp. 4656–4659, 1998.
- [68] F. L. Deepak, C. P. Vinod, K. Mukhopadhyay, A. Govindaraj, and C. N. R. Rao, "Boron nitride nanotubes and nanowires," *ACS Nano*, vol. 4, no. 6, pp. 2979–2993, 2002.
- [69] R. Liu, J. Li, G. Zhou, J. Wu, B. L. Gu, and W. Duan, "Formation, morphology, and effect of complex defects in boron nitride nanotubes: An ab initio calculation," *J. Phys. Chem. C*, vol. 115, pp. 12782–12788, 2011.
- [70] K. Dhungana and R. Pati, "Boron Nitride Nanotubes for Spintronics," *Sensors*, vol. 14, pp. 17655–17685, 2014.
- [71] A. P. Suryavanshi, M. F. Yu, J. G. Wen, C. C. Tang, and Y. Bando, "Elastic modulus and resonance behavior of boron nitride nanotubes," *Appl. Phys. Lett.*, vol. 84, pp. 2527–2530, 2004.
- [72] M. Ghorbani-Asl, N. Zibouche, M. Wahiduzzaman, A. F. Oliveira, A. Kuc, and T. Heine, "Electromechanics in MoS<sub>2</sub> and WS<sub>2</sub>: nanotubes vs. monolayers," *Sci. Rep.*, vol. 3, p. 2961, 2013.
- [73] T. Lorenz, D. Teich, J.-O. Joswig, and G. Seifert, "Theoretical Study of the Mechanical Behavior of Individual TiS<sub>2</sub> and MoS<sub>2</sub> Nanotubes," *J. Phys. Chem. C*, vol. 116, pp. 11714–11721, 2012.
- [74] L. Scheffer, R. Rosentzveig, A. Margolin, R. Popovitz-Biro, G. Seifert, S. R. Cohen, and R. Tenne, "Scanning tunneling microscopy study of WS<sub>2</sub> nanotubes," *Phys. Chem. Chem. Phys.*, vol. 4, pp. 2095–2098, 2002.
- [75] J. C. Slater and G. F. Koster, "Simplified LCAO Method for the Periodic Potential Problem," *Phys. Rev.*, vol. 94, no. 6, pp. 1498–1524, Jun. 1954.
- [76] D. N. Langenberg and R. F. Peart, "Solid-State Physics.," *Science*, vol. 144, pp. 1365–1366, 1964.
- [77] N. Ashcroft and D. Mermin, *Solid State Physics*. 1976.
- [78] R. Evarestov, *Quantum Chemistry of Solids. The LCAO First Principles Treatment of Crystals*. 2007.
- [79] Q. Cui and M. Elstner, "Density functional tight binding: values of semi-empirical methods in an ab initio era.," *Phys. Chem. Chem. Phys.*, vol. 16, no. 28, pp. 14368–77, Jul. 2014.
- [80] M. Elstner, D. Porezag, G. Jungnickel, J. Elsner, M. Haugk, T. Frauenheim, S. Suhai, and G. Seifert, "Self-consistent-charge density-functional tight-binding method for simulations of complex materials properties," *Physical Review B*, vol. 58. pp. 7260–7268, 1998.
- [81] T. Frauenheim, G. Seifert, M. Elstner, Z. Hajnal, G. Jungnickel, D. Porezag, S. Suhai, and R. Scholz, "A self-consistent charge density-functional based tight-binding method for predictive materials simulations in physics, chemistry and biology," *Phys. Status Solidi B-Basic Solid State Phys.*, vol. 217, pp. 41–62, 2000.

- [82] M. Wahiduzzaman, A. F. Oliveira, P. Philipsen, L. Zhechkov, E. van Lenthe, H. A. Witek, and T. Heine, "DFTB Parameters for the Periodic Table: Part 1, Electronic Structure," *J. Chem. Theory Comput.*, vol. 9, no. 9, pp. 4006–4017, Sep. 2013.
- [83] W. Kohn and L. J. Sham, "Self-consistent equations including exchange and correlation effects," *Phys. Rev.*, vol. 140, no. 4A, p. A1133, 1965.
- [84] V. Schönfeld, "Spherical Harmonics," 2005. [Online]. Available: <http://www.ncbi.nlm.nih.gov/pubmed/22002379>.
- [85] G. Dolgonos, B. Aradi, N. H. Moreira, and T. Frauenheim, "An improved self-consistent-charge density-functional tight-binding (SCC-DFTB) set of parameters for simulation of bulk and molecular systems involving titanium," *J. Chem. Theory Comput.*, vol. 6, pp. 266–278, 2010.
- [86] A. N. Rudenko and M. I. Katsnelson, "Quasiparticle band structure and tight-binding model for single- and bilayer black phosphorus," *Phys. Rev. B*, vol. 89, no. 20, p. 201408, May 2014.
- [87] Y. Takao and A. Morita, "Electronic structure of black phosphorus: Tight binding approach," *Phys. B+C*, vol. 105, no. 1–3, pp. 93–98, May 1981.
- [88] Y. Takao, H. Asahina, and A. Morita, "Electronic Structure of Black Phosphorus in Tight Binding Approach," *J. Phys. Soc. Japan*, vol. 50, no. 10, pp. 3362–3369, Oct. 1981.
- [89] V. Sorkin and Y. W. Zhang, "The structure and elastic properties of phosphorene edges," *Nanotechnology*, vol. 26, no. 23, p. 235707, Jun. 2015.
- [90] V. Sorkin and Y. W. Zhang, "The deformation and failure behaviour of phosphorene nanoribbons under uniaxial tensile strain," *2D Mater.*, vol. 2, no. 3, p. 035007, 2015.
- [91] H. J. Monkhorst and J. D. Pack, "Special points for Brillouin-zone integrations," *Phys. Rev. B*, vol. 13, no. 12, pp. 5188–5192, Jun. 1976.
- [92] J. D. Pack and H. J. Monkhorst, "'special points for Brillouin-zone integrations'-a reply," *Physical Review B*, vol. 16, pp. 1748–1749, 1977.
- [93] R. Luschtinetz, A. F. Oliveira, J. Frenzel, J.-O. Joswig, G. Seifert, and H. A. Duarte, "Adsorption of phosphonic and ethylphosphonic acid on aluminum oxide surfaces," *Surf. Sci.*, vol. 602, no. 7, pp. 1347–1359, Apr. 2008.
- [94] M. Gaus, X. Lu, M. Elstner, and Q. Cui, "Parameterization of DFTB3/3OB for Sulfur and Phosphorus for Chemical and Biological Applications.," *J. Chem. Theory Comput.*, vol. 10, no. 4, pp. 1518–1537, Apr. 2014.
- [95] D. J. Chadi and M. L. Cohen, "Special points in the brillouin zone," *Phys. Rev. B*, vol. 8, pp. 5747–5753, 1973.

- [96] D. Sánchez-Portal, E. Artacho, J. Soler, A. Rubio, and P. Ordejón, "Ab initio structural, elastic, and vibrational properties of carbon nanotubes," *Phys. Rev. B*, vol. 59, no. 19, pp. 12678–12688, 1999.
- [97] O. Gülseren, T. Yildirim, and S. Ciraci, "Systematic ab initio study of curvature effects in carbon nanotubes," *Phys. Rev. B*, vol. 65, no. 15, p. 153405, 2002.
- [98] a. Pullen, G. Zhao, D. Bagayoko, and L. Yang, "Structural, elastic, and electronic properties of deformed carbon nanotubes under uniaxial strain," *Phys. Rev. B*, vol. 71, p. 205410, 2005.
- [99] a. Kis and a. Zettl, "Nanomechanics of carbon nanotubes," *Philos. Trans. R. Soc. A Math. Phys. Eng. Sci.*, vol. 366, no. 1870, pp. 1591–1611, 2008.
- [100] E. S. Penev, V. I. Artyukhov, F. Ding, and B. I. Yakobson, "Unfolding the Fullerene: Nanotubes, Graphene and Poly-Elemental Varieties by Simulations," *Adv. Mater.*, vol. 24, pp. 4956–4976, 2012.
- [101] P. Zhang, Y. Huang, P. H. Geubelle, P. a. Klein, and K. C. Hwang, "The elastic modulus of single-wall carbon nanotubes: A continuum analysis incorporating interatomic potentials," *Int. J. Solids Struct.*, vol. 39, no. 13–14, pp. 3893–3906, 2002.
- [102] J. P. Lu, "Elastic properties of carbon nanotubes and nanoropes," *Phys. Rev. Lett.*, vol. 79, no. 7, pp. 1297–1300, 1997.
- [103] D. H. Robertson, D. W. Brenner, and J. W. Mintmire, "Energetics of nanoscale graphitic tubules," *Phys. Rev. B*, vol. 45, no. 21, pp. 12592–12595, 1992.
- [104] K. N. Kudin, G. E. Scuseria, and B. I. Yakobson, "C<sub>2</sub>F, BN, and C nanoshell elasticity from ab initio computations," *Phys. Rev. B*, vol. 64, p. 235406, 2001.
- [105] E. Hernández, C. Goze, P. Bernier, a. Rubio, and E. Hernandez, "Elastic Properties of C and B<sub>x</sub>C<sub>y</sub>N<sub>z</sub> Composite Nanotubes," *Phys. Rev. Lett.*, vol. 80, no. 20, pp. 4502–4505, 1998.
- [106] M. M. J. Treacy, T. W. Ebbesen, and J. M. Gibson, "Exceptionally high Young's modulus observed for individual carbon nanotubes," *Nature*, vol. 381, pp. 678–680, 1996.
- [107] V. N. Popov, V. E. Van Doren, and M. Balkanski, "Elastic properties of single-walled carbon nanotubes," *Phys. Rev. B*, vol. 61, no. 4, pp. 3078–3084, 2000.
- [108] M. Gaus, Q. Cui, and M. Elstner, "DFTB3: Extension of the self-consistent-charge density-functional tight-binding method (SCC-DFTB)," *J. Chem. Theory Comput.*, vol. 7, pp. 931–948, 2011.
- [109] F. Caruso, D. R. Rohr, M. Hellgren, X. Ren, P. Rinke, A. Rubio, and M. Scheffler, "Bond breaking and bond formation: How electron correlation is captured in many-body perturbation theory and density-functional theory," *Phys. Rev. Lett.*, vol. 110, no. April, p. 146403, 2013.

